Supplemental Material: Effects of surface rigidity and metallicity on dielectric properties and ion interactions at aqueous hydrophobic interfaces

Philip Loche,[1,2] Laura Scalfi,[2,3] Mustakim Ali Amu,[3] Otto Schullian,[2]
Douwe J. Bonthuis,[4] Benjamin Rotenberg,[3] and Roland R. Netz[2,*]

[1] *Laboratory of Computational Science and Modeling, IMX, École Polytechnique Fédérale de Lausanne, 1015 Lausanne, Switzerland*
[2] *Fachbereich Physik, Freie Universität Berlin, 14195 Berlin, Germany*
[3] *Physicochimie des Électrolytes et Nanosystèmes Interfaciaux, CNRS 8234, Sorbonne Université, F-75005 Paris, France*
[4] *Institute of Theoretical and Computational Physics, Graz University of Technology, 8010 Graz, Austria*

CONTENTS

S1. METHODS

A. Insulating planar interfaces

Simulations for graphene, water vapor and hexane are performed using the GROMACS molecular dynamics simulation package [1], the water bond lengths are constrained using the SETTLE algorithm [2] and the integration time step is set to $\Delta t = 2\,\mathrm{fs}$, using a velocity rescale thermostat, including a stochastic factor [3] at 300 K with a time constant of 0.5 ps. Simulation boxes are periodically replicated in all directions and long-range electrostatics are handled using the smooth particle mesh Ewald (SPME) technique. For the graphene and the water vapor system a slab correction according to Ref. [4] is used. A slab correction is not applicable for the hexane systems since the approximate slab correction method requires a vacuum layer at least 3 times larger than the system. Lennard-Jones interactions are cut off at a distance $r_{\mathrm{cut}} = 0.9\,\mathrm{nm}$. The total simulation time for the extraction of dielectric profiles was at least 100 ns and we provide our analysis library MAICoS (located at `https://gitlab.com/maicos-devel/maicos`), based on MDAnalysis [5], for the extraction of the dielectric profiles [6–8]. The graphene-water interaction potential is taken from the GROMOS53A6 force field [9]. We validate this choice by computing contact angles of SPC/E water on graphene for a range of ϵ_{CO} around the GROMOS value of $\epsilon_{CO} = 0.42469$ kJ/mol, at a fixed $\sigma_{\mathrm{CO}} = 0.33670$ nm. For

* rnetz@physik.fu-berlin.de

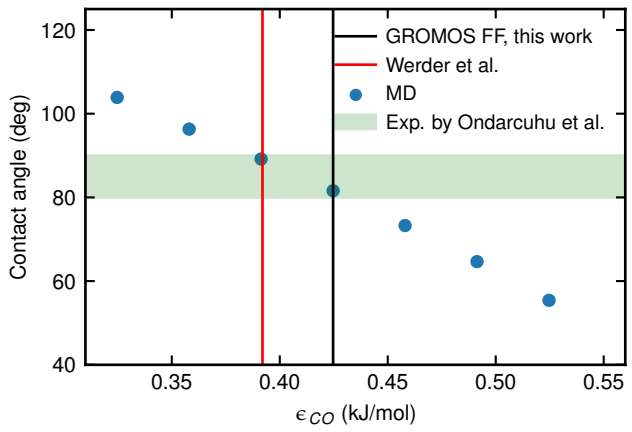

Figure S1. Contact angle dependence of a drop of SPC/E water on a graphite sheet as a function of the parameter ϵ_{CO}, compared to the experimental value of $85^\circ \pm 5^\circ$ given in Ref. [12].

these calculations, we use a $2.56 \times 30.25 \times 60.00\,\mathrm{nm}^3$ box with a graphene sheet composed of 2952 carbon atoms in the xy plane and a cylindrical droplet in the x-direction of different sizes, varying from 1183 to 8842 water molecules, following the procedure in Ref. [11]. The simulations are equilibrated for 2.2 ns and the production phase lasts 198 ns. As shown in Fig. S1, the GROMOS force field parameters reproduce experimental contact angles of water on graphene within the experimental precision [12]. The red vertical line corresponds to the $\epsilon_{CO} = 0.392$ kJ/mol value of Werder et al. [10], in which the σ_{CO} is different, equal to 0.3190 nm.

For hexane we use a modified OPLS all-atom force field [13]. The ions parameters are obtained by Weerasinghe and Smith [14] and optimized for the ion interaction with bulk water but also reproduce ion profiles at the water-vapor interface well [15]. For all cross terms, we use Lorentz-Berthelot combination rules.

Additionally, to avoid movement of the water slab relative to the fixed ions in the water vapor system, the center of mass of the system is constrained to its initial position by a harmonic potential with a force constant $k = 1000\,\mathrm{kJ\,mol^{-1}nm^{-2}}$. We use a constraining procedure that takes the periodicity of the system properly into account when water molecules in the vapor phase jump across the system's periodic boundary [16]. The constraint on the water phase has no effect on interfacial properties as shown earlier [17]. Note that we do not apply a constraint to the hexane-water system since here the movement of the water slab is negligible.

B. Water concentration in vapor and hexane phase

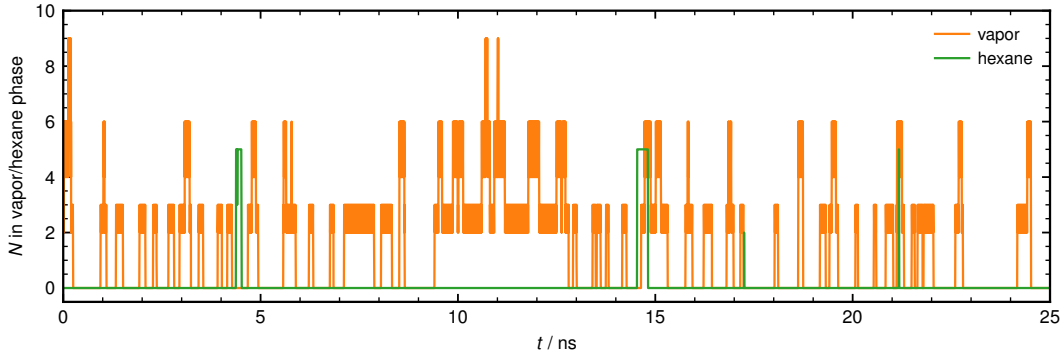

Figure S2. Time-dependent number of water molecules N in the vapor and hexane phase, respectively. The time series shows the first 25 ns of each trajectory. The total time of the water-vapor trajectory is 1 μs and of the water-hexane trajectories is 600 ns.

Figure S2 shows the time-dependent number of water molecules N in the vapor and hexane phase, respectively. The average number of water molecules is $N_{\mathrm{vap}} = 1.13$ in vapor and $N_{\mathrm{hex}} = 0.068$ in hexane. The volume of the vapor phase is $V_{\mathrm{vap}} = 1604\,\mathrm{nm}^3$ and the volume of the hexane phase is $V_{\mathrm{hex}} = 115\,\mathrm{nm}^3$. The partial pressure of the water in each phase is obtained from the mean water number density by using the ideal gas law $P = Nk_{\mathrm{B}}T/V$.

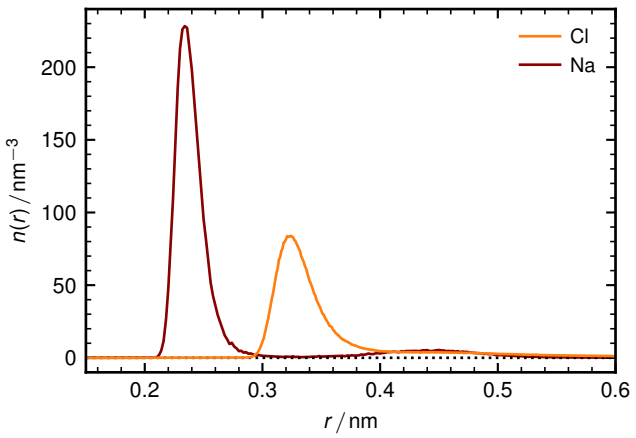

Figure S3. Radial oxygen density $n(r)$ around a single chloride and a single sodium ion in the vapor phase. The density is calculated on the same trajectories as shown in Fig. 3e.

C. Water Density around Ions in Vapor Phase

In Fig. S3 we show the radial oxygen density around a single ion in the vapor phase. We find that most water molecules are located within a single hydration shell. Additionally, we find a slight hump in the density around the sodium ion, indicative of a very weak second hydration shell, which is absent for the chloride ion. From $n(r)$ we calculate the number of water molecules around each ion according to

$$N = 4\pi \int_0^{1\,\mathrm{nm}} \mathrm{d}r\, r^2 n(r)\,. \tag{S1}$$

We obtain $N_{\mathrm{Na}} = 5.9$ and $N_{\mathrm{Cl}} = 6.9$ in agreement with our findings in the main text.

D. Metallic graphite simulations

For simulations of metallic graphite, we use constant potential simulations as implemented in the molecular dynamics code MetalWalls [18]. Metallic graphite atoms bear a Gaussian charge distribution of fixed width $\eta^{-1} = 0.56\,\text{Å}$, centered on the carbon atoms. Their magnitude is determined at each time step to enforce the constant potential constraint at the nuclei position and a global electroneutrality constraint using a matrix inversion method [19]. In contrast, the charges on the water atoms and ions are constant and create a fluctuating field that determines the polarization charges at the metallic surface atoms at each time step. We use two-dimensional boundary conditions (no periodicity in the z direction), with 2D Ewald summation to compute electrostatic interactions in the presence of the Gaussian-distributed charges [20, 21]. Simulations are run with a time step of 2 fs and the temperature is set to 300 K using a Nosé-Hoover chain thermostat. We use the same force field parameters as for water-graphene simulations, but bond lengths are constrained using the RATTLE algorithm. Biased simulations are run using the coupling of MetalWalls with PLUMED [22, 23]. Each biased simulation is equilibrated for at least 100 ps and then run for 10 ns. Simulations of non-metallic graphite are run with the same parameters and settings except that the graphite charges are kept fixed equal to zero.

E. Thermodynamic integration and umbrella sampling

For obtaining the free energy of the test ion we place the ion, with zero charge and LJ parameters, at fixed positions inside the system. The TI calculations are done in two steps: First all Lennard-Jones interactions between the test ion and all other atoms are gradually turned on. Note that for calculating the Lennard-Jones contribution to the free energy no counter ion is present. In the second step the charges of the test and the oppositely charged counter ion are increased from $q = 0$ to ± 1 (measured in units of the elementary charge). The integration is performed along an alchemical reaction coordinate λ, where $\lambda = 0$ corresponds to the initial (A) and $\lambda = 1$ to the final state (B). For the integration the Hamiltonian is interpolated linearly $H(\lambda) = (1-\lambda)H_A + \lambda H_B$. Free energy differences are calculated by integrating $\langle \partial H/\partial\lambda \rangle = \langle H_B - H_A \rangle$ from $\lambda = 0$ to $\lambda = 1$ using the alchemical-analysis toolkit [24]. For the integration of the Lennard-Jones potential, we use a soft-core potential to prevent a singularity at $\lambda = 0$ with a

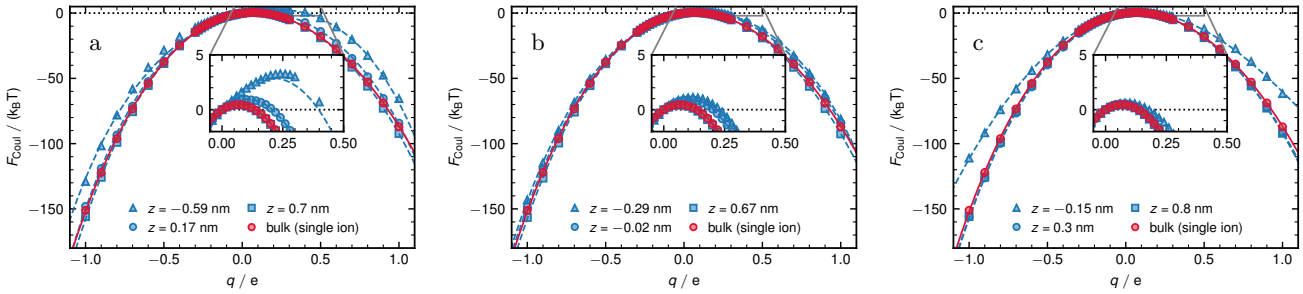

Figure S4. Coulomb part of the ion solvation free energy F_{Coul} for different separations from the surfaces represented by different blue symbols. Red symbols show results for an ion in a periodic bulk water box. Lines are fits according to Eq. (S3). Data is shown for a) water vapor, b) hexane and c) graphene.

soft-core radius $\alpha = 0.5\,\mathrm{nm}$ and a soft-core power $p = 1$. The Lennard-Jones transformation is divided into 10 steps and the charging transformation into 22 so that the actual charge in each step is $q' = \lambda q$. The simulation time for each λ state is at least 5 ns and up to 50 ns, and we neglect the first 500 ps for equilibration. This procedure allows to separate straightforwardly the Lennard-Jones and Coulomb contributions of the free energy of the test ion. The Coulomb part of the free energy calculated from the simulations contains contributions from the test and the counter ion. To obtain the free energy of only the test ion, F_{Coul}, we subtract the solvation energy of the isolated counter ion, F_{counter}, obtained from separate bulk simulations, the analytically calculated electrostatic interaction between test and counter ions, F_{int}, as well as the interaction of the test ion with its periodic images, F_{pbc}, from the simulated free energy

$$F_{\mathrm{Coul}} = F_{\mathrm{sim}} - F_{\mathrm{counter}} - F_{\mathrm{int}} - F_{\mathrm{pbc}}\,. \tag{S2}$$

The interaction is calculated analytically from the potential $\Phi(\boldsymbol{r})$ created by the counter ion $F_{\mathrm{int}} = q_{\mathrm{test}}\Phi(\boldsymbol{r})$ where q_{test} is the valency of the test charge positioned at $\boldsymbol{r}$. $\Phi(\boldsymbol{r})$ is given in Eq. (S46) of our previous work [25]. For the subtraction of the periodic-image contribution F_{pbc} we use analytic expressions [25, 26], as explained in detail in the Supplementary Section of Ref. 17.

To extract the linear and non-linear contributions we expand F_{Coul} in powers of the charge[25]

$$F_{\mathrm{Coul}}(z) = \Phi(d)z + A(d)z^2 + B(z)q^3 + C(z)q^4 \tag{S3}$$

and obtain the coefficients from fitting the polynomial to the simulation data at several positions z. The necessary free energy for $|q| < 1$, required for a reasonable fit, can be directly extracted without creating additional trajectories. This is achieved by recalculating the term $\partial H/\partial\lambda = H_A - H_B(q)$ for each different final state B (corresponding to different final q values) by rerunning the trajectory, since in the original runs only the energies for H_A corresponding to $q = 0$ and H_B corresponding to $q = 1$ are stored by GROMACS. The fits according to Eq. (S3) are done in a sequential fitting procedure as described previously[25]. Example fits are shown for all systems and a few different ion positions in Figure S4.

The free energy profiles for metallic and non-metallic graphite systems are obtained from umbrella sampling simulations using the Weighted Histogram Analysis Method[27] (WHAM). In the umbrella sampling simulations, we introduce a harmonic biasing potential on the distance z between the chloride ion and the first graphite atomic plane, $w(z) = \frac{k}{2}(z - z_{\mathrm{ref}})^2$, using the PLUMED library [22, 23] interfaced with the molecular simulation code MetalWalls. The different biasing windows are specified in Table S1.

Table S1. Reference position z_{ref} and spring constant k for the various windows used for umbrella sampling.

z_{ref} (nm)	0.2	0.2	0.2	0.2	0.2	0.2	0.4	0.6	0.8	1.0	1.2	1.4	1.6
k (kJ/(mol nm^2))	500	5,000	20,000	50,000	100,000	200,000	250	250	250	250	250	250	250

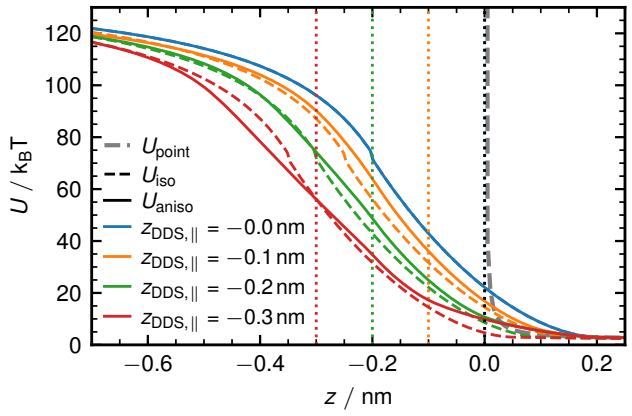

Figure S5. Image-charge repulsion of a monovalent spherical ion with radius $R = 0.254$nm in water ($\varepsilon = 70$) from the vapor phase ($\varepsilon = 1$). Solid lines show the tensorial 3-region model U_{aniso}, given in Eqs. (S57) – (S60) of the Supplemental Information of our previous work [25], with an interfacial slab characterized by $\varepsilon_\parallel = 70$ and $\varepsilon_\perp = 1$, $z_{\text{DDS},\perp} = 0$ and different values of $z_{\text{DDS},\parallel}$ as given in the legend. Dashed lines correspond to the isotropic 2-region model with U_{iso} given by Eq. (S5), where the interface between the two dielectric media is located at $z_{\text{DDS}} = (z_{\text{DDS},\perp} + z_{\text{DDS},\parallel})/2$. The gray dashed line depicts the result from the point charge model as given in Eq. S6 with the dielectric interface at $z = 0$. Vertical dotted lines depict the position of $z_{\text{DDS},\parallel}$.

F. Definition of dividing surface positions

For obtaining the positions of the dividing surfaces (DS) we use

$$z^{DS} = z_I + \int_{z_I}^{z_{II}} \frac{f(z_{II}) - f(z)}{f(z_{II}) - f(z_I)} \mathrm{d}z, \tag{S4}$$

where $f(z)$ is the respective profile (density, dielectric response or electrostatic potential) and z_I and z_{II} are positions in the two bulk phases.

S2. FREE ENERGY OF A UNIFORMLY CHARGED SPHERICAL SHELL

For determining the polarization energy of a spherical ion at a single sharp dielectric interface, which defines the 2-region model, we describe the ion as a uniformly charged spherical shell with a surface charge density $\sigma = q/(4\pi R^2)$, where R is the radius of the sphere. The dielectric constant inside the sphere is the same as that of the environment. The polarization energy was previously derived [26] and reads

$$U_{\text{iso}}(\lambda, x) = \frac{q_A^2}{8\pi\varepsilon_0\varepsilon_2 R}\, u(\lambda, x)\,, \tag{S5}$$

where $x = z/R$ is the rescaled separation from the interface and $\lambda = (\epsilon_2 - \epsilon_1)/(\epsilon_1 + \epsilon_2)$ is the dielectric contrast. One finds

$$u(\lambda, x \geq 1) = 1 + \frac{\lambda}{2x} \tag{S6}$$

$$u(\lambda, |x| < 1) = \left(\frac{1}{1-\lambda}\right)\left\{1 - \frac{\lambda x}{2}(1-\lambda) - \lambda^2\left[I_A(x) + I_B(x)\right]\right\} \tag{S7}$$

$$u(\lambda, x \leq -1) = \left(\frac{1+\lambda}{1-\lambda}\right)\left(1 + \frac{\lambda}{2x}\right)\,, \tag{S8}$$

where

$$I_A(x) = \frac{1}{\pi\sqrt{2}} \int_{-x}^{1} \mathrm{d}(\cos\theta) \int_{-1}^{x} \mathrm{d}(\cos\theta') \frac{K\left[\frac{2\sin\theta\sin\theta'}{1-\cos(\theta+\theta')+2x(\cos\theta-\cos\theta'+x)}\right]}{\sqrt{1-\cos(\theta+\theta')+2x(\cos\theta-\cos\theta'+x)}} \tag{S9}$$

$$I_B(x) = \frac{1}{\pi\sqrt{2}} \int_{-x}^{1} \mathrm{d}(\cos\theta) \int_{-1}^{x} \mathrm{d}(\cos\theta') \frac{K\left[\frac{2\sin\theta\sin\theta'}{1+\cos(\theta-\theta')}\right]}{\sqrt{1+\cos(\theta-\theta')}} \tag{S10}$$

(S11)

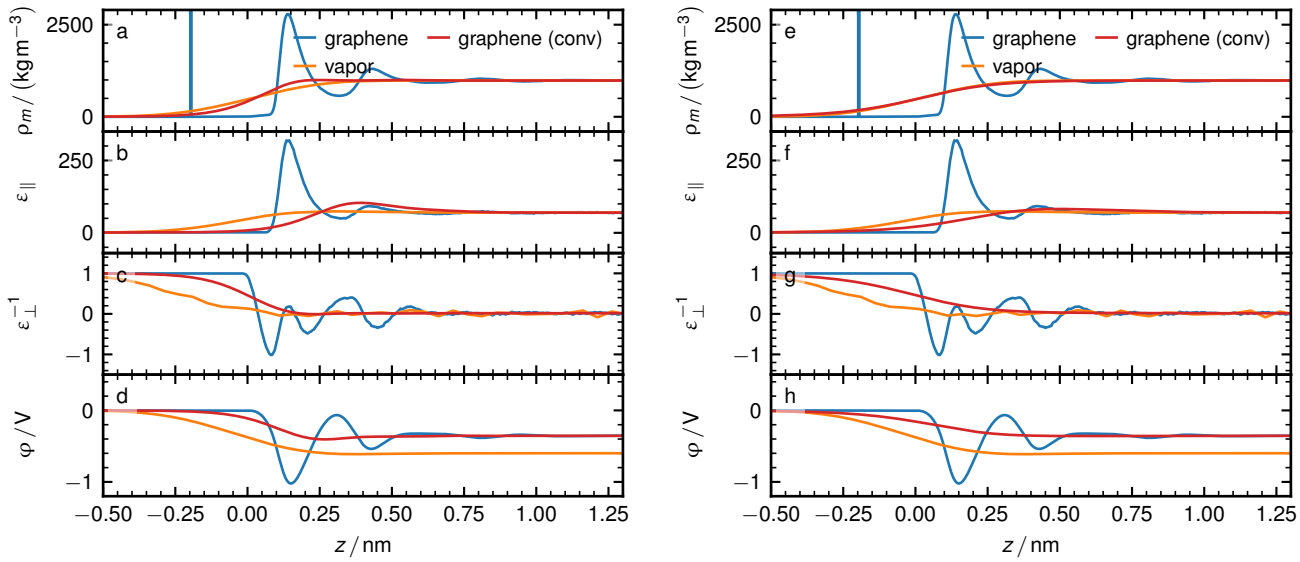

Figure S6. Mass density $\rho_m(z)$, dielectric $\epsilon(z)$ and potential $\varphi(z)$ profiles from Fig. 1 in the main text for graphene-water (blue) and vapor-water (orange). The red line shows convoluted graphene profiles according to Eq. (S15) for (a-d) an interfacial width of $w = 0.36\,\mathrm{nm}$; and (e-h) an interfacial width of $w = 0.6\,\mathrm{nm}$.

are integrals in terms of the complete elliptic integral of the first kind,

$$K[m] = \int_0^{\pi/2} \frac{\mathrm{d}\alpha}{\sqrt{1 - m^2 \sin^2 \alpha}} \,. \tag{S12}$$

Eq. (S5) is shown in Fig. S5 as dashed lines together with the more complex tensorial 3-region model from our previous work [25], shown as solid lines. The location of the dielectric interface for the 2-region model is chosen as $z_{\mathrm{DDS}} = (z_{\mathrm{DDS},\perp} + z_{\mathrm{DDS},\parallel})/2$ [25], which leads to good agreement with the tensorial 3-region model.

S3. CONVOLUTED GRAPHENE PROFILES

Here we demonstrate that the water-vapor interfacial profiles can be approximately described by convoluting the graphene profiles with an interface-position distribution. Following Sedlmeier *et al.* [28], an interfacial profile $f(z)$ for an arbitrary observable at the water-vapor interface can be described by

$$f(z) = \frac{f_r + f_l}{2} + \frac{f_r - f_l}{2} \tanh\left(\frac{2z}{w}\right) \,, \tag{S13}$$

where f_l and f_r are the bulk values in the left and right half spaces and w is the interfacial width. We take $f'(z)/(f_r - f_l)$ as the normalized interface position distribution $P(z)$ and obtain

$$P(z) = \frac{1}{w}\left[1 - \tanh^2\left(\frac{2z}{w}\right)\right] \,. \tag{S14}$$

Based on Eq. (S14) we construct the convoluted profile according to

$$f_{\mathrm{conv}}(z) = \int \mathrm{d}z' P(z') f(z - z') \,. \tag{S15}$$

Figure S6 shows mass density $\rho_m(z)$, dielectric $\epsilon(z)$ and potential $\varphi(z)$ profiles for graphene-water and vapor-water from Fig. 1 in the main text, compared with the convoluted graphene profiles for two choices of the interfacial width w. In Fig. S6a–d, we use an interfacial width of $w = 0.36\,\mathrm{nm}$, which is the expected interfacial broadening for a system with a lateral area of $5.1\,\mathrm{nm} \times 5.4\,\mathrm{nm}$, similar to our setup [28]. We find rather good agreement for the density profile

Table S2. Estimate of the rescaled translational entropy for chloride and sodium ions S_{trans} as given in Eq.(S18) in the vapor and hexane phase.

	Vapor	Hexane
Cl^-	10.85	10.67
Na^+	11.04	10.85

but rather poor results for the dielectric and the potential profiles. In Fig. S6e–h, we choose a slightly larger interfacial width of $w = 0.6$ nm and find almost perfect agreement between the water-vapor and the convoluted graphene density profiles, also the agreement for the dielectric profiles has improved. For the potential profiles, the convoluted profiles reproduce the shape, but the potential value far away from the interface differs substantially between the vapor-water and the graphene-water results.

S4. WATER BINDING MODEL

The ion-hydrogen distance $B_{\mathrm{H},i}$ is estimated using the SPC/E water model geometry [29] as

$$B_{\mathrm{H,Cl}} = \sqrt{B_{\mathrm{O,Cl}}^2 + r_{\mathrm{OH}}^2 - 2B_{\mathrm{O,Cl}} r_{\mathrm{OH}} \cos\alpha} \tag{S16}$$

$$B_{\mathrm{H,Na}} = \sqrt{B_{\mathrm{O,Na}}^2 + r_{\mathrm{OH}}^2 + 2B_{\mathrm{O,Na}} r_{\mathrm{OH}} \cos\alpha}, \tag{S17}$$

where $r_{\mathrm{OH}} = 0.1\,\mathrm{nm}$ is the oxygen hydrogen distance and $\alpha = 54.735°$ is half of the hydrogen-oxygen-hydrogen bond angle. In Table S2 we give the exact values of the translational entropy

$$S_{\mathrm{trans}} = \ln\left(\frac{v_{\mathrm{naq},j}}{v_{\mathrm{hyd},i}}\right), \tag{S18}$$

where $v_{\mathrm{hyd},i}$ denotes the effective volume available to a water molecule that is bound to the ion of type i and $v_{\mathrm{naq},j}$ is the molecular volume of a water molecule in the non-aqueous phase of type j (either vapor or hexane).

S5. COMPARISON OF ELECTROSTATIC INTERFACIAL POTENTIALS

In Fig. S7, we provide a comparison between the laterally averaged electrostatic potential $\varphi(z)$ calculated from the charge distribution via

$$\varphi(z) = -\frac{1}{\varepsilon_0}\int_{-\infty}^{z} \mathrm{d}z' \int_{-\infty}^{z'} \rho(z'')\,\mathrm{d}z'' \tag{S19}$$

and the potential $\Phi(z)$ acting on an ion obtained from the expansion of the free energy in powers of the ion charge in Eq. (5) in the main text. We provide both the unshifted potentials (left) and the potentials shifted to zero in the bulk phase.

S6. ION HYDRATION STRUCTURE AT THE TIP4P/ε-VAPOR INTERFACE

To assess the influence of the water model on our results, we run similar simulations as in the main text using the TIP4P/ε water model [30] instead of the SPC/E water model. In these simulations, the ion is fixed in the vapor phase ($z < 0$) at different positions. Figure S8a shows a snapshot of a water finger that forms for a distance between the ion and the GDS of 1.2 nm. We observe small differences in the water-finger stability: while for the TIP4P/ε water model a water finger forms for $z = -1.2$ nm and breaks for $z = -2.1$ nm, for the SPC/E water model at $z = 2.1$ nm the water finger is still present [17]. This may originate in the higher surface tension of $68.4\,\mathrm{mN\,m^{-1}}$ [30] of the TIP4P/ε compared to $64.5\,\mathrm{mN\,m^{-1}}$ [31] of the SPC/E model. The surface tension of water (experimental value $71.96\,\mathrm{mN\,m^{-1}}$ [32]) is fairly well reproduced by both water models, but it would be interesting to use polarizable force fields in the future (for example, the surface tension of the MB-pol water model is $66.82\,\mathrm{mN\,m^{-1}}$ [32]).

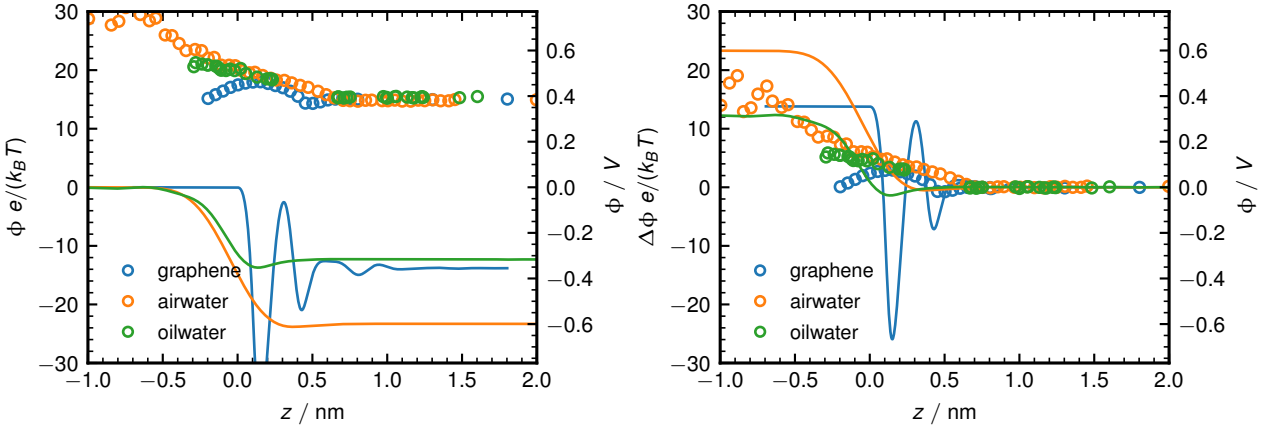

Figure S7. Laterally averaged electrostatic potential $\varphi(z)$ calculated by integrating twice over the charge density ρ as given in Eq. (S19) (solid lines), compared to the potential acting on an ion $\Phi(z)$ obtained from a fit of the ionic free energy as given in Eq. (5) (open circles). The left panel shows the unshifted potentials whereas in the right panel the potentials are shifted such that they are zero in liquid water bulk. Data is shown for the graphene (blue), water vapor (orange) and hexane (green) interfaces.

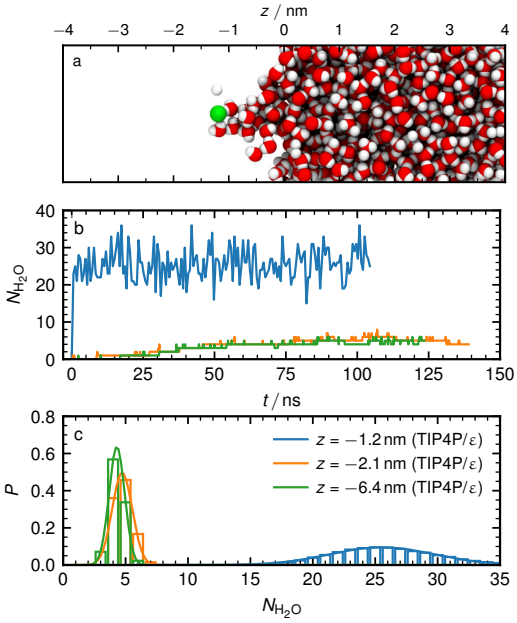

Figure S8. Simulation results using the TIP4P/ε water model. (a) Snapshot of the water configuration around a chloride ion in the vapor phase at a distance $z = -1.2\,\mathrm{nm}$ after 10 ns. (b) Number of water molecules $N_{\mathrm{H_2O}}$ in a sphere with radius 1 nm around the chloride ion at different fixed positions as a function of time. (c) Corresponding distributions of $N_{\mathrm{H_2O}}$, discarding the initial 75 ns. Lines are Gaussian fits.

Figure S8b-c shows the number of water molecules $N_{\mathrm{H_2O}}$ in a sphere with radius 1 nm around a chloride ion as a function of time for different positions and the resulting distributions P for simulations with the TIP4P/ε water model. For the two larger distances, we find that a chloride ion accumulates 4.7 water molecules for $z = -2.1\,\mathrm{nm}$ and 4.3 water molecules for $z = -6.4\,\mathrm{nm}$, which is smaller but comparable to the 6.9 water molecules for the SPC/E model for $z = -7.0\,\mathrm{nm}$ described in the main text and shown in Fig. 3. Also this deviation between the water models is consistent with the difference in surface tension between the two water models.

[1] M. J. Abraham, T. Murtola, R. Schulz, S. Páll, J. C. Smith, B. Hess, and E. Lindahl, GROMACS: High performance molecular simulations through multi-level parallelism from laptops to supercomputers, SoftwareX 10.1016/j.softx.2015.06.001 (2015).
[2] S. Miyamoto and P. A. Kollman, Settle: An analytical version of the SHAKE and RATTLE algorithm for rigid water models, Journal of Computational Chemistry 10.1002/jcc.540130805 (1992).
[3] G. Bussi, D. Donadio, and M. Parrinello, Canonical sampling through velocity rescaling, The Journal of Chemical Physics

10.1063/1.2408420 (2007).
[4] I.-C. Yeh and M. L. Berkowitz, Ewald summation for systems with slab geometry, The Journal of Chemical Physics http://dx.doi.org/10.1063/1.479595 (1999).
[5] N. Michaud-Agrawal, E. J. Denning, T. B. Woolf, and O. Beckstein, MDAnalysis: A toolkit for the analysis of molecular dynamics simulations, Journal of Computational Chemistry 10.1002/jcc.21787 (2011).
[6] D. J. Bonthuis, S. Gekle, and R. R. Netz, Profile of the static permittivity tensor of water at interfaces: Consequences for capacitance, hydration interaction and ion adsorption, Langmuir 10.1021/la2051564 (2012).
[7] A. Schlaich, E. W. Knapp, and R. R. Netz, Water Dielectric Effects in Planar Confinement, Phys. Rev. Lett. 10.1103/PhysRevLett.117.048001 (2016).
[8] P. Loche, A. Wolde-Kidan, A. Schlaich, D. J. Bonthuis, and R. R. Netz, Comment on "Hydrophobic Surface Enhances Electrostatic Interaction in Water", Phys. Rev. Lett. 10.1103/PhysRevLett.123.049601 (2019).
[9] C. Oostenbrink, A. Villa, A. E. Mark, and W. F. V. Gunsteren, A biomolecular force field based on the free enthalpy of hydration and solvation: The GROMOS force-field parameter sets 53A5 and 53A6, Journal of Computational Chemistry 10.1002/jcc.20090 (2004).
[10] T. Werder, J. H. Walther, R. L. Jaffe, T. Halicioglu, and P. Koumoutsakos, On the Water-Carbon Interaction for Use in Molecular Dynamics Simulations of Graphite and Carbon Nanotubes, The Journal of Physical Chemistry B **107**, 1345 (2003).
[11] S. Carlson, M. Becker, F. N. Brünig, K. Ataka, R. Cruz, L. Yu, P. Tang, M. Kanduč, R. Haag, J. Heberle, H. Makki, and R. R. Netz, Hydrophobicity of Self-Assembled Monolayers of Alkanes: Fluorination, Density, Roughness, and Lennard-Jones Cutoffs, Langmuir **37**, 13846 (2021).
[12] T. Ondarçuhu, V. Thomas, M. Nuñez, E. Dujardin, A. Rahman, C. T. Black, and A. Checco, Wettability of partially suspended graphene, Scientific Reports **6**, 24237 (2016).
[13] S. W. I. Siu, K. Pluhackova, and R. A. Böckmann, Optimization of the OPLS-AA Force Field for Long Hydrocarbons, J. Chem. Theory Comput. 10.1021/ct200908r (2012).
[14] S. Weerasinghe and P. E. Smith, A Kirkwood–Buff derived force field for sodium chloride in water, The Journal of Chemical Physics 10.1063/1.1622372 (2003).
[15] S. I. Mamatkulov, C. Allolio, R. R. Netz, and D. J. Bonthuis, Orientation-Induced Adsorption of Hydrated Protons at the Air–Water Interface, Angewandte Chemie International Edition 10.1002/anie.201707391 (2017).
[16] O. Engin, A. Villa, M. Sayar, and B. Hess, Driving Forces for Adsorption of Amphiphilic Peptides to the Air-Water Interface, J. Phys. Chem. B 10.1021/jp1024922 (2010).
[17] P. Loche, D. J. Bonthuis, and R. R. Netz, Molecular dynamics simulations of the evaporation of hydrated ions from aqueous solution, Commun Chem 10.1038/s42004-022-00669-5 (2022).
[18] A. Marin-Laflèche, M. Haefele, L. Scalfi, A. Coretti, T. Dufils, G. Jeanmairet, S. K. Reed, A. Serva, R. Berthin, C. Bacon, S. Bonella, B. Rotenberg, P. A. Madden, and M. Salanne, MetalWalls: A classical molecular dynamics software dedicated to the simulation of electrochemical systems, Journal of Open Source Software 10.21105/joss.02373 (2020).
[19] L. Scalfi, D. T. Limmer, A. Coretti, S. Bonella, P. A. Madden, M. Salanne, and B. Rotenberg, Charge fluctuations from molecular simulations in the constant-potential ensemble, Phys. Chem. Chem. Phys. (2020).
[20] S. K. Reed, O. J. Lanning, and P. A. Madden, Electrochemical interface between an ionic liquid and a model metallic electrode, J. Chem. Phys. 10.1063/1.2464084 (2007).
[21] T. R. Gingrich and M. Wilson, On the Ewald summation of Gaussian charges for the simulation of metallic surfaces, Chem. Phys. Lett. 10.1016/j.cplett.2010.10.010 (2010).
[22] M. Bonomi, G. Bussi, C. Camilloni, G. A. Tribello, P. Banáš, A. Barducci, M. Bernetti, P. G. Bolhuis, S. Bottaro, D. Branduardi, R. Capelli, P. Carloni, M. Ceriotti, A. Cesari, H. Chen, W. Chen, F. Colizzi, S. De, M. De La Pierre, D. Donadio, V. Drobot, B. Ensing, A. L. Ferguson, M. Filizola, J. S. Fraser, H. Fu, P. Gasparotto, F. L. Gervasio, F. Giberti, A. Gil-Ley, T. Giorgino, G. T. Heller, G. M. Hocky, M. Iannuzzi, M. Invernizzi, K. E. Jelfs, A. Jussupow, E. Kirilin, A. Laio, V. Limongelli, K. Lindorff-Larsen, T. Löhr, F. Marinelli, L. Martin-Samos, M. Masetti, R. Meyer, A. Michaelides, C. Molteni, T. Morishita, M. Nava, C. Paissoni, E. Papaleo, M. Parrinello, J. Pfaendtner, P. Piaggi, G. Piccini, A. Pietropaolo, F. Pietrucci, S. Pipolo, D. Provasi, D. Quigley, P. Raiteri, S. Raniolo, J. Rydzewski, M. Salvalaglio, G. C. Sosso, V. Spiwok, J. Šponer, D. W. H. Swenson, P. Tiwary, O. Valsson, M. Vendruscolo, G. A. Voth, A. White, and The PLUMED consortium, Promoting transparency and reproducibility in enhanced molecular simulations, Nature Methods 10.1038/s41592-019-0506-8 (2019).
[23] G. A. Tribello, M. Bonomi, D. Branduardi, C. Camilloni, and G. Bussi, PLUMED 2: New feathers for an old bird, Computer Physics Communications 10.1016/j.cpc.2013.09.018 (2014).
[24] P. V. Klimovich, M. R. Shirts, and D. L. Mobley, Guidelines for the analysis of free energy calculations, J Comput Aided Mol Des 10.1007/s10822-015-9840-9 (2015).
[25] P. Loche, C. Ayaz, A. Schlaich, D. J. Bonthuis, and R. R. Netz, Breakdown of Linear Dielectric Theory for the Interaction between Hydrated Ions and Graphene, J. Phys. Chem. Lett. 10.1021/acs.jpclett.8b02473 (2018).
[26] M. N. Tamashiro and M. A. Constantino, Ions at the Water-Vapor Interface, J. Phys. Chem. B 10.1021/jp911898t (2010).
[27] Grossfield, Alan, WHAM: The weighted histogram analysis method, version 2.0.10.2.
[28] F. Sedlmeier, D. Horinek, and R. R. Netz, Nanoroughness, Intrinsic Density Profile, and Rigidity of the Air-Water Interface, Phys. Rev. Lett. 10.1103/PhysRevLett.103.136102 (2009).
[29] H. J. C. Berendsen, J. R. Grigera, and T. P. Straatsma, The missing term in effective pair potentials, J. Phys. Chem. 10.1021/j100308a038 (1987).
[30] R. Fuentes-Azcatl and J. Alejandre, Non-Polarizable Force Field of Water Based on the Dielectric Constant: TIP4P/epsilon,

J. Phys. Chem. B 10.1021/jp410865y (2014).
[31] F. Chen and P. E. Smith, Simulated surface tensions of common water models, J. Chem. Phys. 10.1063/1.2745718 (2007).
[32] S. K. Reddy, S. C. Straight, P. Bajaj, C. Huy Pham, M. Riera, D. R. Moberg, M. A. Morales, C. Knight, A. W. Götz, and F. Paesani, On the accuracy of the MB-pol many-body potential for water: Interaction energies, vibrational frequencies, and classical thermodynamic and dynamical properties from clusters to liquid water and ice, The Journal of Chemical Physics **145**, 194504 (2016).